

Variable-Stiffness Control of a Dual-Segment Soft Robot Using Depth Vision

Jiewen Lai^{ID}, Student Member, IEEE, Bo Lu^{ID}, and Henry K. Chu^{ID}, Member, IEEE

Abstract—A soft-bodied robot exhibits prominent dexterity due to the soft nature of its material. However, the softness can become a burden when the robot needs to interact with the environment, given that the targeted object is usually much stiffer than the compliant soft robot. A variable-stiffness soft robot, fusing the merits of softness and stiffness, is in favor of many applications, such as robot-assisted minimally invasive surgeries. In this article, we propose a tendon-tensioning method to adaptively control the stiffness of a dual-segment tendon-driven backboneless soft robot based on depth vision. A depth-vision-based closed-loop controller is designed for stiffness compensation when the manipulator is subjected to the external load. Experiments were conducted to examine the feasibility and performance of the proposed method. The results confirm our control scheme on the robot with controllability of stiffness up to 132%. Based on our method, the manipulator with an external payload can follow designated trajectories with positioning errors reduced up to 50% comparing to that with open-loop control. Without quantifying the instantaneous stiffness, this work contributes a generalized method for tuning the stiffness of the tendon-driven soft robots in the presence of external disturbances without onboard sensing.

Index Terms—RGB-D perception, soft robot, soft robot materials and design, tendon/wire mechanism, visual servoing.

I. INTRODUCTION

SOFT robots are usually made from soft-touch materials [1]. The motion of the robot manipulator, which has theoretically infinite degrees of freedom (DOF), can be generated by the elastic deformation of the soft body. With multisegment articulated from one to another, the manipulator can work in sinuous surroundings, such as a snake. The low Young's modulus of soft material endows the robot to interact with humans safely, which is one of the development trends in robotics.

Manuscript received January 19, 2021; revised April 4, 2021; accepted April 22, 2021. This work was supported by HK PolyU under Grant 4-RKCM. Recommended by Technical Editor H. Wang and Senior Editor G. Alici. (*Corresponding author: Henry K. Chu*)

Jiewen Lai and Henry K. Chu are with the Department of Mechanical Engineering, The Hong Kong Polytechnic University, Hong Kong (e-mail: jw.lai@connect.polyu.hk; henry.chu@polyu.edu.hk).

Bo Lu is with the CUHK T Stone Robotics Institute, The Chinese University of Hong Kong, Hong Kong (e-mail: bolu@cuhk.edu.hk).

This article has supplementary material provided by the authors and color versions of one or more figures available at <https://doi.org/10.1109/TMECH.2021.3078466>.

Digital Object Identifier 10.1109/TMECH.2021.3078466

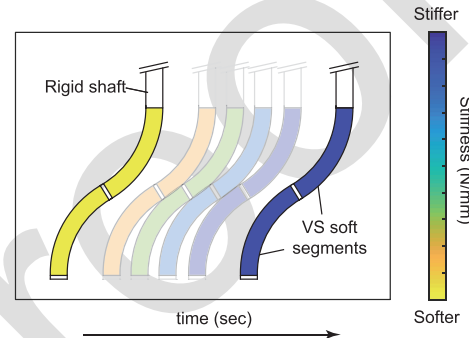


Fig. 1. Conceptual schematic of a variable-stiffness dual-segment soft robot. The manipulator is stiffened with an imperceptible change of its pose.

Robot-assisted minimally invasive surgery (R-MIS) involves a lot of interactions between humans (patients) and robots [2], and soft robots become the most promising candidates. For instance, a soft or continuum robotic manipulator can be used as a surgical forceps to manipulate the soft and fragile tissues [2], [3]. To ensure the safety, it is desired that the manipulator can be soft enough to minimize the harm to the anatomical structure in case of collision. On the contrary, the manipulator should provide sufficient stiffness for physical manipulation, such as grasping and ablation [4]–[6]. If the manipulator is too soft, undesired deformation during the physical interaction would increase the challenge in controlling the end-effector. Therefore, it leads to a demand for developing variable-stiffness soft robots that can switch from the flexible state to the rigid state, and reversible if needed [7]. A schematic of the variable-stiffness soft robot is given in Fig. 1.

A. Related Works

In elastic stability theory, the flexural stiffness ($K_b = E_b I$) of a beam can be quantified by the ability to resist bending in a plane of symmetry [8]. It can be expressed by the product of Young's modulus in bending (E_b) and the second moment of area (I). Therefore, varying the stiffness of a soft manipulator basically requires the adjustment on either the material intrinsic properties (E_b) or the structural geometry (I). The employments of changing stiffness by controlling intrinsic material properties in soft robots and biomedical devices have been reported in [9]–[11]. However, the mechanism sacrifices the output force and activation time, which is hence unqualified for the tasks demanding manipulation in a subsecond response.

TABLE I
COMPARISON OF VARIABLE-STIFFNESS CONTINUUM MANIPULATORS IN THE LITERATURE

Continuum Body	Ref.	Body Material(s)	Actuation	Diameter (mm)	Bendable Segments	Stiffening Method
Rigid components	[20]	Ti6Al4V & Steel spring	Cable/Tendon	28	1	Cable tensioning
	[21]	Aluminum & Epoxy	Cable/Tendon	12	1	Cable tensioning
	[22]	3D-printed ABS	Cable/Tendon	20	2	Cable tensioning
	[12]	Granular & Membrane	Pneumatic	15	-	Granular jamming
Soft body	[11]	Silicone	Hydraulic	13 (semicircle)	1	Low-melting-point-alloy
	[13]	Nylon fibers	Pneumatic	16	-	Fiber jamming
	[14]	Silicone & Ground coffee	Hydraulic	25–32	1	Granular jamming
	[15]	Latex rubber & Mylar	Pneumatic	24	1	Layer jamming
	[23]	Silicone (STIFF-FLOP)	Pneumatic & Cable	23	1	Cable tensioning
	Ours	3D-printed elastomer	Cable/Tendon	9	2	Cable tensioning

69 Aim at developing a variable-stiffness manipulator with fast
70 response, a number of researchers have been working on de-
71 signing delicate jamming structures for soft/continuum manip-
72 ulators. The granular jamming mechanism changes the manip-
73 ulator's stiffness by modifying the interactions of embedded
74 granular particles, e.g., glass beads [12], fiber [13], or even
75 ground coffee [14]. The particles are free-to-flow within the
76 manipulator structure during normal operations, but they are
77 interlocked when the vacuum is applied. This innovative idea
78 requires a substantial internal volume for granular beads to
79 achieve a sufficient stiffness. The mechanism is unlikely to adopt
80 a compact design that spares a hollow passage for MIS instru-
81 ments. To overcome this problem, several other jamming meth-
82 ods have been proposed. The layer jamming mechanism [15],
83 [16] is capable of tuning the manipulator stiffness by making
84 use of the controllable friction between the multilayer skins
85 by changing the layerwise air pressure. Similar concepts us-
86 ing different mediums have been proposed [17], [18]. Zhong
87 *et al.* [19] designed a bistable rigid joint for a soft robot to
88 produce a locking mechanism for stiffness variation. The afore-
89 mentioned solutions innovate from the perspective of robot de-
90 sign, which require fabrications of complicated continuum robot
91 prototypes.

92 Nevertheless, the adjustable rigidity soft robots can be real-
93 ized using pure actuation methods. Shiva *et al.* [23] proposed an
94 approach to control the stiffness of a silicone-based pneumat-
95 ically driven soft robot by actuating the vinelike tendons that
96 adhere to the outer layer in an antagonistic way, opposing the
97 pneumatic actuation. The hybrid actuation scheme allows one to
98 control the robot pose and stiffness simultaneously. However, it
99 is a common limitation that the pneumatic-driven soft robots are
100 having a relatively large diameter ($\phi 23$ mm in [23] and $\phi 32$ mm
101 in [24]) as they need bulky air chambers for pressurization [2].

102 Changing the gap or spacing within the robot structure through
103 the tendon/cable-driven mechanism is an alternative to downsize
104 the variable-stiffness continuum manipulator [24]. In [22], a pure
105 cable-driven continuum robot based on stacking of multiple rigid
106 arched disks was capable of tuning its stiffness by tensioning the
107 cables along with the robot asymmetrically. Tamadon *et al.* [20]
108 developed a rigid-bodied continuum manipulator for implant
109 delivery in cardiac valve delivery. The $\phi 28$ -mm single-segment
110 robot was featured with the functions of tip positioning and
111 configuration locking by controlling the cable tension. Choset
112 *et al.* [21] developed a highly articulated robotic probe, also a
113 flexible device assembled using rigid components, which can be

stiffened by cable tensioning. Utilizing the cable-driven mech-
anism, they downscaled the diameter of the continuum probe
to 12 mm. These cable-actuated manipulators allow compact
designs with a hollow passage in a considerable volume (sizes of
conventional laparoscopic surgical instruments vary from 3 to 5
mm [22]). For the ease of reading, we list some variable-stiffness
continuum robots in Table I.

B. Contribution

During the operation, the continuum robot is often required to
carry a load, leading to an additional deformation on the body.
In order to retain the original pose, it is desired to adjust the
stiffness with respect to the load. In this work, the stiffness
adjustment on a two-segment soft robot is achieved through the
tendon tensioning method. Compared with the aforementioned
studies, our robot adopts a backboneless structure to improve
the body deformability. As a result, the tensioning would im-
prove the bending and axial stiffness to cancel out the load.
The experimental results indicate that the current end-effector
position and the robot configuration would affect the robot
stiffness, increasing the challenges in evaluating the required
stiffness based on the load. To overcome this problem, this
work proposes a scheme to correlate the tendon forces, in the
form of displacements, with the relative end-effector position.
Based on the feedback from a depth camera, the required tension
force is adaptively adjusted to compensate for the deviation that
caused by the load. Experiments were conducted to verify that
the proposed tendon-tensioning method can stiffen the overall
soft manipulator from a soft state to a stiffened state without
excessive deviation in the configuration. Different end-effector
trajectories were examined to evaluate the tip positioning accu-
racy under various loads. This work extends our prior works
that allows the configuration control of a dual-segment soft
robot in a 2-D space [25]. The contributions of this work are as
follows:

- 1) We develop a miniature soft-bodied dual-segment con-
tinuum manipulator with variable stiffness. The vari-
able stiffness is realized by using the proposed tendon-
tensioning control method, which benefits a compact
robot design, and enables the soft robot to stabilize its
planned motion by compensating for external forces.
- 2) We propose a tendon-tensioning method that provides an
additional DOF, the manipulator's stiffness, for control.
The feasibility is supported by extensive experiments.

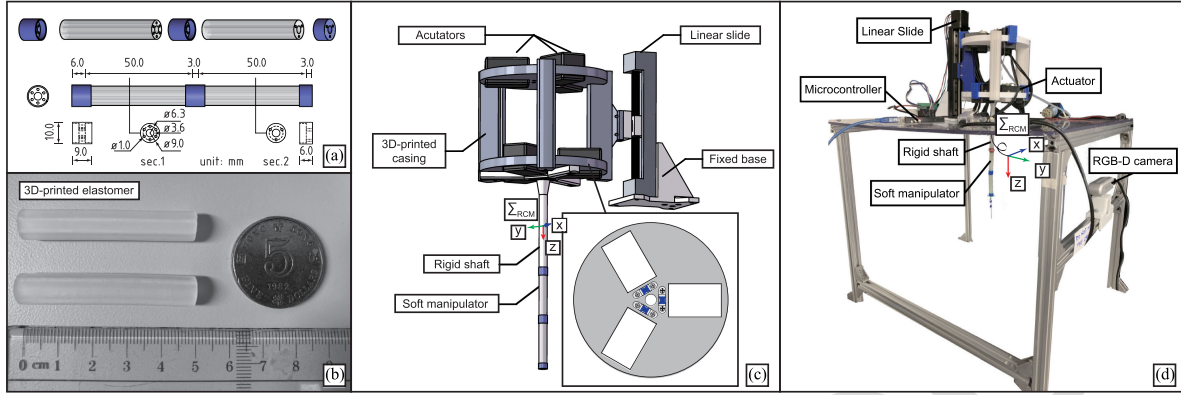


Fig. 2. (a) Design layout of the soft manipulator and its assembly. (b) Snapshot of 3-D printed soft segments. (c) Robot assembly. (d) Overall setup.

By employing the eye-to-hand RGB-D visual sensing, the manipulator is capable of adaptively tuning its stiffness only, which depends on the spatial perception of the end-effector. Without quantifying the instantaneous stiffness, we contribute a generalized method for tuning the stiffness of the tendon-driven soft-bodied robots in the presence of external disturbances without onboard sensing.

II. PROTOTYPE DESCRIPTION AND METHOD

A. Prototype Description

The layout of our dual-segment soft robot and the stereolithography-based 3-D printed soft segments are demonstrated in Fig. 2(a) and (b). The soft body was made from Agilus30 (Stratasys, Ltd., Eden Prairie, MN, USA) PolyJet photopolymer. The manipulator is composed of two different segments of the same size. The distal segment contains three equidistantly distributed passages for tendons, whereas the proximal segment has six in total. Each soft segment is 50 mm in length with an outer diameter of 9 mm. A $\phi 3.6$ -mm lumen, which is adequate to fit an aspirator tube or a flexible endoscope, is reserved at the axial center. The soft manipulator was driven by six tendons that wired along the passages of the body and tied at the disks, and the total weight of the manipulator is 5.2 g. The assembly of the robot is shown in Fig. 2(c). To manipulate the robot, each tendon was connected to a Dynamixel XM430-W350 actuator (ROBOTIS, Seoul, South Korea) through a fixed pulley, and these actuators were secured on a 3-D printed fixture. To provide an additional translational DOF, we mounted the fixture on a linear slide with its moving direction perpendicular to the ground. The translational DOF configures a remote center of motion (RCM) mechanism, which is widely used in R-MIS to physically bound the motion to a point to mechanically reduce the risk of tearing the incision port and gain higher dexterity [26], [27]. The details concerning the prototype can be found in our previous work [28] and the supplement video.

As depicted in Fig. 2(d), a depth camera (RealSense D435) was mounted at a side, forming an eye-to-hand system, to perceive the spatial position of the labeled points of interest (POIs). A Kanade–Lucas–Tomasi tracker was employed to enhance the

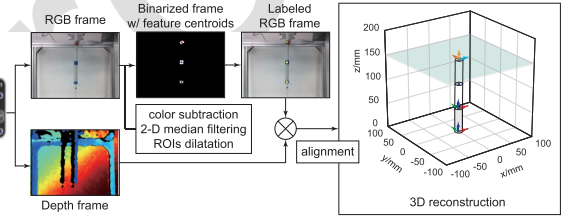


Fig. 3. RGB-D-based visual tracking and the manipulator's 3-D reconstruction.

tracking stability of registered features in successive frames. In our case, the tracking system was hosted by a laptop with a 16-GB RAM CPU, allowing real-time tracking at around 20 ft/s in 640×480 p live stream. We set the world coordinate frame at a fixed spatial point as the origin of Σ_{RCM} , which is 50 mm away from the base of the proximal soft segment when the translational DOF is at zero, with its \hat{z} -axis points to the distal end and \hat{y} -axis aligns toward the camera. The coordinate of the end-effector with respect to (w.r.t.) Σ_{RCM} can be calculated by homogeneous matrix transformations. The framewise workflow of image processing is shown in Fig. 3. The hand–eye calibration was performed to reduce the mechanical and installation error. Images are enhanced for keypoint tracking. The resolution of the POIs is 0.001 mm on the X- and Z-axis (RGB module), and 1 mm on the Y-axis (depth module). The accuracy of image plane was within 0.1 mm, and that of the depth was <2% within 2 m according to the camera specification. The tendon calibration was based on the 3-D reconstruction and the default position of the POIs (base, intermediate, and tip position). The first step was to ensure that the aforementioned three points were aligned to the desired location as much as possible. After that, each cable was individually tested by actuating the same displacement, and the knots were manually adjusted to ensure symmetric robot motion in six directions.

B. Kinematics Modeling

Assumption: By following the tendon-driven mechanism, as introduced in Section II-A, the robot kinematic model can be geometrically derived under the following assumptions.

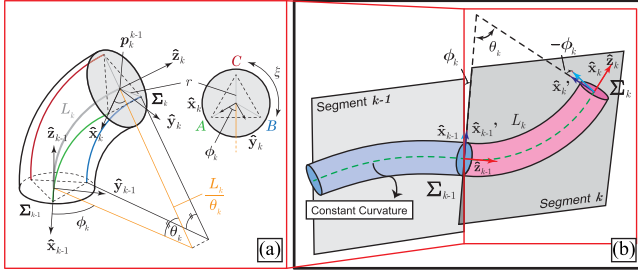


Fig. 4. Geometry assignment of the PCC model. (a) k th segment. (b) Consecutive segments of the k th and the $(k-1)$ th.

- 224 1) Each soft segment bends as a circular arc within a certain
225 range [3], [29].
- 226 2) Gravitational energy is neglected since the elastic potential
227 energy dominates the gravity.
- 228 3) Rigid disks are assumed to be infinitely thin, so that the
229 distal end of the tendons are perpendicular to the disks.
- 230 4) Actuation tendons are inextensible.

In a dual-segment continuum manipulator system, the actuator space \mathbf{q} can be expressed by $\mathbf{q} = [q_1 \ q_2]^\top \in \mathbb{R}^{6 \times 1}$, and the actuation for the k th subsegment, where $k \in \{1, 2\}$, is $\mathbf{q}_k = [q_{k,1} \ q_{k,2} \ q_{k,3}]^\top$, representing three actuation tendons for one segment. Without over deflection, a multisegment continuum manipulator can be closely approximated by a finite set of consecutive constant curvatures geometrically in free space, which is widely known as piecewise constant curvature (PCC) assumption [3]. The PCC simplifies each segment to a 2-DOF system—each inextensible segment (L_k , a constant) can be bent on its own plane (θ_k), and a twist (ϕ_k) can be attained between neighboring segments (see Fig. 4). For each segment, a twisting motion around its axial axis (\hat{z}_k), which is not achievable by tendon actuation, is neglected. The aforementioned description concludes the spatial configuration of the k th segment (ψ_k) as $\psi_k = [\theta_k \ \phi_k]^\top$, where $\theta_k \in [0, \theta_{\max}]$ and $\phi_k \in (-\pi, \pi]$. Therefore, the distal tip position of the k th segment w.r.t. the $(k-1)$ th segment can be derived as

$$\mathbf{p}_k^{k-1} = \begin{bmatrix} \mathbf{x}_k \\ \mathbf{y}_k \\ \mathbf{z}_k \end{bmatrix} = \frac{L_k}{\theta_k} \begin{bmatrix} (1 - c_{\theta_k}) c_{\phi_k} \\ (1 - c_{\theta_k}) s_{\phi_k} \\ s_{\theta_k} \end{bmatrix} \quad (1)$$

where $c(\cdot)$ and $s(\cdot)$ are the abbreviations for $\cos(\cdot)$ and $\sin(\cdot)$, respectively. The configuration of the k th segment w.r.t. its base (ψ_k) can be derived from (1) as

$$\psi_k = \begin{bmatrix} \theta_k \\ \phi_k \end{bmatrix} = \begin{bmatrix} 2 \arccos \frac{\|\mathbf{z}_k\|}{\|\mathbf{p}_k^{k-1}\|_2} \\ \arctan \frac{\mathbf{y}_k}{\mathbf{x}_k} \end{bmatrix} \quad (2)$$

where $\|\cdot\|_2$ is the Euclidean norm. Under the assumption of inextensible tendons, one can geometrically [see Fig. 4(a)] define the relation between the specific tendon actuation ($q_{k,i}$) and the segment configuration (ψ_k)

$$q_{k,i} = -\theta_k r c_{[\phi_k + (i-1)\xi]} \quad (3)$$

where $i \in \{1, 2, 3\}$ indicates the numbered tendon A, B, C , and $\xi = \frac{2\pi}{3}$ represents the trisection angle of circle. The negative sign notes a pulling (tensioning) motion. The radius of the tendon distribution is r . Taking the time derivative of (3) yields

$$\dot{\mathbf{q}}_k = \begin{bmatrix} -rc_{\phi_k} & r\theta_k s_{\phi_k} \\ -rc_{\phi_k+\xi} & r\theta_k s_{\phi_k+\xi} \\ -rc_{\phi_k+2\xi} & r\theta_k s_{\phi_k+2\xi} \end{bmatrix} \begin{bmatrix} \Delta\theta_k \\ \Delta\phi_k \end{bmatrix} \quad (4)$$

where $\mathbf{J}_{kq\psi}$ is the Jacobian matrix that maps the actuation and configuration of the k -segment, and $\dot{\psi}_k$ can be approximately treated as the change of (2) in instantaneous kinematics. It should be noted that

$$\sum_{i=1}^3 \dot{q}_{k,i} = 0. \quad (5)$$

On the basis of (3), the mapping between tendon actuation and manipulator configuration can be attained as follows [3]:

$$\theta_k = \frac{2\sqrt{q_{k,1}^2 + q_{k,2}^2 + q_{k,3}^2 - q_{k,1}q_{k,2} - q_{k,1}q_{k,3} - q_{k,2}q_{k,3}}}{3r} \quad (6)$$

$$\phi_k = \text{atan2}(3(q_{k,2} - q_{k,3}), \sqrt{3}(q_{k,2} + q_{k,3} - 2q_{k,1})) \quad (7)$$

where $\text{atan2}(s_\phi, c_\phi)$ computes the four-quadrant inverse tangent of s_ϕ and c_ϕ such that $\phi \in (-\pi, \pi]$.

To this end, the analytical solution of manipulator actuation to assigned tip pose can be ideally derived as $\mathbf{q}_k = f_{\text{inv}}(\mathbf{p}_k^{k-1})$, in which $f_{\text{inv}}(\cdot)$ is the inverse mapping from the segment tip to the segment actuation in the k th segment.

As demonstrated in Fig. 4, the orientation of the k th segment tip w.r.t. its base is determined by three sequential rotations: rotating ϕ_k around the \hat{z}_{k-1} -axis, rotating θ_k around the \hat{y}_{k-1} -axis, and rotating ϕ_k reversely around the \hat{z}_k -axis of the current tip frame to ensure the torsionless assumption within each segment. Hence, the rotation matrix of the k th segment (\mathbf{R}_k^{k-1}) can be expressed by

$$\begin{aligned} \mathbf{R}_k^{k-1} &= \text{Rot}(\hat{z}_{k-1}, \phi_k) \cdot \text{Rot}(\hat{y}_{k-1}, \theta_k) \cdot \text{Rot}(\hat{z}_k, -\phi_k) \\ &= \begin{bmatrix} c_{\phi_k}^2 c_{\theta_k} + s_{\phi_k}^2 & c_{\phi_k} s_{\phi_k} (c_{\theta_k} - 1) & c_{\phi_k} s_{\theta_k} \\ c_{\phi_k} s_{\phi_k} (c_{\theta_k} - 1) & s_{\phi_k}^2 c_{\theta_k} + c_{\phi_k}^2 & s_{\phi_k} s_{\theta_k} \\ -c_{\phi_k} s_{\theta_k} & -s_{\phi_k} s_{\theta_k} & c_{\theta_k} \end{bmatrix} \end{aligned} \quad (8)$$

where the operator $\text{Rot}(\hat{\mathbf{u}}_k, \delta)$ denotes the rotation matrix of rotating angle (δ) along the unit axis of the k th segment ($\hat{\mathbf{u}}_k$).

For our dual-segment manipulator system, we use the notation t for tip, m for middle point (which is also the tip of the proximal segment), and b for base. The position of tip frame w.r.t. the stationary RCM can be obtained as

$$\mathbf{p}_t^{\text{RCM}} = \mathcal{H} + \mathbf{p}_m^b + \mathbf{R}_m^b \mathbf{p}_t^m \quad (9)$$

where $\mathcal{H} = [0 \ 0 \ h]^\top$ represents the translation DOF in axial direction w.r.t. the RCM.

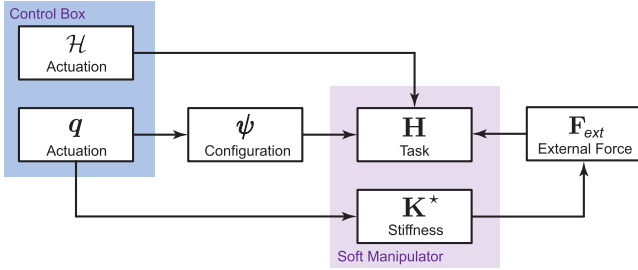


Fig. 5. Mapping of the proposed soft robot system. The actuation space is also responsible to the robot stiffness.

C. Stiffness Variation

Natural soft tissue exhibit a self-protective mechanism against external forces exerted on the body: being soft at small strains, and rapidly stiffened at higher strains to prevent damage. In this work, we propose a *bioinspired* method that learns from such stress-stiffening behavior of natural soft tissues [30]. We employ this idea to contribute a variable-stiffness soft robot with a better control under large strains that caused by the external forces.

Assume the soft manipulator to be a virtual spring in free space with an initial stiffness of \mathbf{K}_q in response of the force of tendons actuation \mathbf{F}_q and a resultant tip displacement s_q in the task space, one gets

$$\mathbf{F}_q = \mathbf{K}_q s_q. \quad (10)$$

In the case where an external force, within the elastic limit of the soft robot, is introduced to the system, and the initial stiffness is not robust enough to resist, (10) shall be revised as

$$\mathbf{F}_q + \mathbf{F}_{\text{ext}} = \mathbf{K}_q (s_q + \Delta u) \quad (11)$$

where \mathbf{F}_{ext} is the external force that applied to the soft manipulator, and Δu is the undesired perturbation of the robot tip. The stiffness of the manipulator \mathbf{K}_q is an actuation-dependent variable: intuitively, a bent segment will be stiffer than the straight segment. With respect to an arbitrary lateral-axial resolution, the external force can be explicitly expressed as

$$\mathbf{F}_{\text{ext}} = \begin{bmatrix} \mathbf{F}_{\text{lt}} \\ \mathbf{F}_{\text{ax}} \end{bmatrix} = \begin{bmatrix} K_{\text{lt}} & 0 \\ 0 & K_{\text{ax}} \end{bmatrix} \begin{bmatrix} \Delta u_{\text{lt}} \\ \Delta u_{\text{ax}} \end{bmatrix} = \mathbf{K}_q \Delta u \quad (12)$$

where $\Delta u_{\text{lt}} = \|\mathbf{x}_{\text{des}} - \mathbf{x}_{\text{cur}}\|_2$ and $\Delta u_{\text{ax}} = \|\mathbf{z}_{\text{des}} - \mathbf{z}_{\text{cur}}\|_2$ represent the spatial deviation in the lateral and axial directions, respectively.

To compensate the perturbation, we apply extra force to the tendons, $\underline{\mathbf{F}}$, as a prestress to the system to obtain a new tip displacement \underline{s} by a displacement compensation of the tip Δc

$$\mathbf{F}_q + \mathbf{F}_{\text{ext}} + \underline{\mathbf{F}} = \underbrace{(\mathbf{K}_q + \underline{\mathbf{K}})}_{\mathbf{K}^*} \underbrace{(s_q + \Delta u - \Delta c)}_{\underline{s}} \quad (13)$$

where $\underline{\mathbf{K}}$ is the additional stiffness matrix gained from the tendon prestress, and \mathbf{K}^* is the optimized manipulator stiffness. The mapping is given in Fig. 5. With the aim of having an accurate tip positioning control, one needs to narrow down the tip error, which is defined by $\|s_q - \underline{s}\|$. Minimizing such error formulates

an optimization problem as

$$\arg \min_{\underline{\mathbf{F}}} \left\| \frac{\mathbf{F}_q}{\mathbf{K}^* - \underline{\mathbf{K}}} - \frac{\mathbf{F}_q + \mathbf{F}_{\text{ext}} + \underline{\mathbf{F}}}{\mathbf{K}^*} \right\|. \quad (14)$$

It has been experimentally found that the mechanical response of the soft elastomer we use is highly nonlinear, and it could be affected by the 3-D printing parameters, such as build orientation [31]. Therefore, it is challenging to precisely formulate a relationship between the tendon actuation and the manipulator's strain. In addition, the external force is usually unknown when without onboard sensors (such as tension sensors [32] for tendon, or strain gauges [33] that adhered/embedded to the soft body). However, with a depth vision provided by the RGB-D camera, the spatial deviation of the POIs (Δu) can be easily acquired. The deviation of POIs can be obtained by other spatial positioning setups (e.g., EM tracking) as well.

Given the assumption that the tendons are inextensible, the actuation force that applied to the tendons can be linearly approximated by a nonzero positive constant α as

$$\begin{cases} \mathbf{F}_q = \alpha \underline{\mathbf{q}} \\ \underline{\mathbf{F}} = \alpha \underline{\mathbf{q}} \end{cases} \quad (15)$$

where $\underline{\mathbf{q}}$ denotes the extra tendon actuation in the form of pulling length. Therefore, (13) can be rewritten as

$$\begin{aligned} \alpha(\mathbf{q} + \underline{\mathbf{q}}) &= (\mathbf{K}_q + \underline{\mathbf{K}})(s_q + \Delta u - \Delta c) - \mathbf{K}_q \Delta u \\ &= \mathbf{K}_q s_q - \mathbf{K}_q \Delta c + \underline{\mathbf{K}} s_q + \underline{\mathbf{K}} \Delta u - \underline{\mathbf{K}} \Delta c \\ &= \mathbf{K}^* s_q - \mathbf{K}^* \Delta c + \underline{\mathbf{K}} \Delta u \end{aligned} \quad (16)$$

where $(\mathbf{q} + \underline{\mathbf{q}})$ denotes the superposition of the tendon actuation, which can be termed as the optimized actuation \mathbf{q}^* . Hence, it gives

$$\mathbf{q}^* = \alpha^{-1} (\mathbf{K}^* s_q - \mathbf{K}^* \Delta c + \underline{\mathbf{K}} \Delta u). \quad (17)$$

On the right-hand side of (17), the first term $\alpha^{-1} \mathbf{K}^* s_q$ represents the designated actuation with a resultant tip motion under optimized stiffness, the second term $-\alpha^{-1} \mathbf{K}^* \Delta c$ denotes the compensation of tip motion, which is generated by optimized stiffness, and the third term $\alpha^{-1} \underline{\mathbf{K}} \Delta u$ is the neglectable deviation, which is arisen by the extra stiffness. If $\underline{\mathbf{K}} = 0$, the initial stiffness shall not provide any compensation and, thus, $\Delta c = 0$, returning $\mathbf{q} = \alpha^{-1} \mathbf{K}_q s_q$, which is the same as the elementary actuation given by (10). According to (17), we can regulate the optimized actuation of tendons. Using an iterative approach to update the actuation at the n th node of the path, one can obtain

$$\underbrace{\mathbf{q}^*}_{\text{optimized}} := \underbrace{\mathbf{q}}_{IK} - \underbrace{\int_0^n \text{sgn}(\mathbf{p}_{t,\text{des}}^{\text{RCM}} - \mathbf{p}_{t,\text{cur}}^{\text{RCM}}) \lambda \mathcal{Q} \mathbf{I} dn}_{\text{stiffening term}} \quad (18)$$

where $\mathbf{q}^* \in \mathbb{R}^{6 \times 1}$ represents the actuation being tuned, and $\mathbf{q} \in \mathbb{R}^{6 \times 1}$ denotes the instantaneous inverse kinematic solution of desired tip pose. $\mathbf{p}_{t,\text{des}}^{\text{RCM}}$ is the desired or current detected tip position w.r.t. the RCM frame. \mathcal{Q} is the tensioning-loosening variable based on the depth visual feedback as

$$\mathcal{Q} = \mu \|\Delta u\|_2, \quad 0 \leq \mathcal{Q} \leq \varepsilon \quad (19)$$

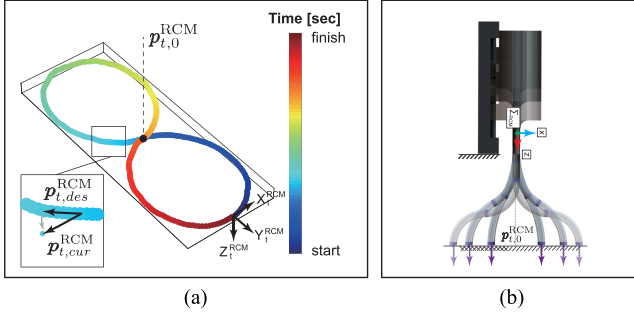


Fig. 6. (a) Typical closed trajectory. (b) Opposite-bending configuration for tip motion decoupling [28].

such that (5) becomes $\sum_{i=1}^3 \dot{q}_{k,i}^* = \text{const.}$, with (6) and (7) still hold, ensuring the robot configuration will not be changed when updating \mathbf{q}^* (will be experimentally examined in Section III-A). We empirically set μ as 0.05 based on the incremental motion of the servo motors. $\mathbf{I} = [1 \ 1 \ 1 \ \frac{1}{2} \ \frac{1}{2} \ \frac{1}{2}]^\top$ is the column vector representing the decoupled actuation tendons for dual-segment robot. Recalling (4), the total Jacobian matrix can be assembled as

$$\mathbf{J}_{q\psi} = \underbrace{\begin{bmatrix} \mathbf{e}_3 & \mathbf{e}_3 \\ \mathbf{e}_3 & \mathbf{0} \end{bmatrix}}_{\mathcal{A}} \begin{bmatrix} \mathbf{J}_{1q\psi} & \mathbf{0} \\ \mathbf{0} & \mathbf{J}_{2q\psi} \end{bmatrix} \in \mathbb{R}^{6 \times 4} \quad (20)$$

where \mathcal{A} represents the actuation coupling matrix between segments, and \mathbf{e}_3 denotes the three-by-three identity matrix for the Jacobian coupling. The pose of the proximal segment shall be corrected together with the distal segment when the distal tip is changing its position through actuating the distal cables that are running through the proximal segment [28]. A buffer scalar λ is assigned to the tensioning term for a smoother transition of the change of stiffness. To determine whether the current state of the manipulator shall be stiffened or loosened, a position-based switch was designed, as shown in Fig. 6(a), and Algorithm 1 based on (21)

$$\operatorname{sgn}(\mathbf{p}_{t,\text{des}}^{\text{RCM}} - \mathbf{p}_{t,\text{cur}}^{\text{RCM}}) \left\{ \begin{array}{ll} > 0, & \text{stiffen} \\ = 0, & \text{maintain} \\ < 0, & \text{loosen} \end{array} \right. \quad (21)$$

When the sign operation returns positive, the tension applied to the soft robot shall be enhanced so as to stiffen the robot to compensate for the deviation from the desired path. On the contrary, the tendons shall be loosened to reduce the overshooting of stiffening, as exceeding tendon actuation would induce noticeable strain along the manipulator's neutral line. With a continuous path $\mathcal{P}_{\text{traj}}$ defined by N nodes, one can update the actuation for each node based on the actuation computed from inverse kinematics. The tip positioning shall be gradually converged to the desired path within a threshold after several loops, depending on the setting. A tendon protection mechanism was set by defining the actuation limits. Once it was triggered, the update would be skipped to prevent the exceeding actuation, which may break the tendons.

Algorithm 1: Adaptive Stiffness by Tuning Tension.

```

Result:  $q^*$ 
1 Initialize  $\varepsilon, \mu, \mathcal{P}_{\text{traj}} \in \mathbb{R}^{3N};$ 
2 Track  $\mathbf{p}_{t,\text{cur}}$  from RGB-D;
3  $n = 1;$ 
4  $\mathbf{q}^* = \mathbf{0};$ 
5 while  $n \leq N$  do
6    $\mathbf{p}_{t,\text{des}} = \mathcal{P}_{\text{traj}}(:, n);$ 
7    $\mathbf{q} = f_{\text{inv}}(\mathbf{p}_{t,\text{des}});$ 
8   if  $\mathbf{q}^* \in [\mathbf{q}_{\text{lowerlimit}}, \mathbf{q}_{\text{upperlimit}}] = 1$  then
9     if  $\|\mathbf{p}_{t,\text{des}} - \mathbf{p}_{t,\text{cur}}\|_2 > \varepsilon$  then
10       get  $q^*$  from Eq. (18);
11    $n := n + 1;$ 

```

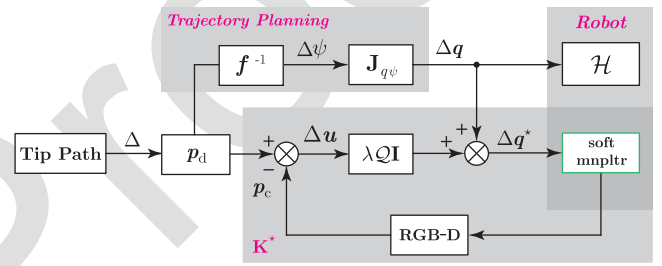


Fig. 7. Block diagram of the stiffness controller for open-loop trajectory tracking tasks.

D. Stiffness Control Using Depth Visual Feedback

389
390
391
392
393
394
395
396
397
398
399
400
401
402
403
404
405
406
407
408
409
410
411
412
413
414
415
416
417
418
419

Tuning the stiffness based on the visual feedback allows the soft manipulator to automatically adjust its stiffness according to the effect caused by the unknown external force at different positions. Based on this understanding, we developed a depth-vision-based method that enables the manipulator to variate its stiffness automatically in a 3-D workspace according to the vectored perturbation of the tip position. The baseline pose, i.e., the desired pose ($\mathbf{p}_d^{\text{RCM}}$), to be compared with is the pose generated from the PCC model.

In end-effector trajectory planning, the user intuitively tends to assign path on a planar work surface, which yields $\mathbf{p}_t^{\text{RCM}} = [\mathbf{x}_t^b, \mathbf{y}_t^b, \epsilon]^\top$, where $\epsilon = \mathbf{z}_t^b + \mathbf{h}$ represents a constant related to the definition of works surface w.r.t. the RCM. Taking the advantage of our two-segment robot design, a special opposite-bending configuration [see Fig. 6(b)] is employed to decouple the tip position and orientation. The configuration shall be confined to $\theta_1 = \theta_2$, where $\theta_k \in (0, \theta_{\max}]$, and $\phi_2 = \phi_1 - \operatorname{sgn}(\phi_1)\pi$, where $\phi_1 \in (-\pi, \pi]$, so that the distal tip can maintain its pointing direction vertically downward in an S-shape posture without losing the mobility in 3-D [28]. The vertically downward pose benefits better stability in the presence of axial loads (see Section III-A), and provides a practical configuration to be used in R-MIS manipulation, such as blood aspiration and surgical site cleaning [28]. A depth-vision-based controller was designed, as shown in Fig. 7, to compute the needed compensation actuation for the robot to conduct planar trajectory tracking with an adaptive stiffness. Therefore, the trajectory planning in the initial tendon actuation and the insertion-retraction stage followed an open-loop control, whereas the stiffness of the soft manipulator adopted the proposed closed-loop tendon-tensioning

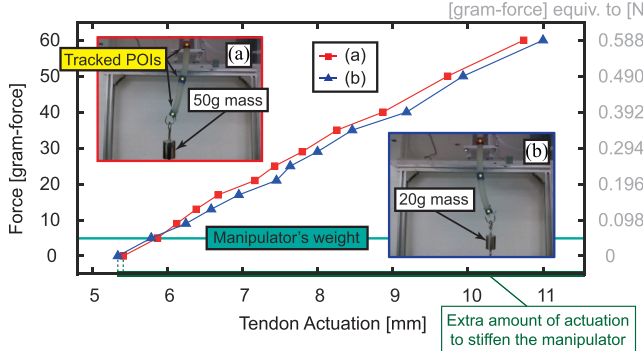


Fig. 8. Manipulator was stiffened by overactuated tendons according to different loads such that the tip can maintain the spatial position of (a) $p_t^{\text{RCM}} \approx [-12, 0148]^T$, and (b) $p_t^{\text{RCM}} \approx [12, 0148]^T$ (unit: mm). The extra amount of tendon actuation represents the additional required tendon displacement that can stiffen the manipulator on top of configuring it to the desired pose.

control based on the depth visual feedback. The corresponding experiments are illustrated in Section III-B.

III. EXPERIMENT

A. Validation of the Stiffening Scheme

In order to examine the change in axial stiffness (K_{ax}), we introduce static load to the robot tip. The basic setup of our testbed is shown in Fig. 2(d). In the experiment, an axial load was given to the manipulator through metal weight. The axial stiffness should be optimized to bear the weight, and thus, the manipulator can maintain the desired pose. As shown in Fig. 8, the relationship between the tendon actuation and the axial force was plotted. The tip was initially configured at a certain position. Then, metals were hooked at the tip, generating an axial force from 5 to 60 gf, to deflect the tip position. The robot body was manually stiffened by applying extra tendon actuation so that the tip can maintain its initial position. The 3-D coordinates of POIs were automatically tracked in real time using an RGB-D camera. The result indicates a linear relationship between tendon actuation and axial load.

For lateral stiffness (K_{lt}), we let the configured manipulator to resist a slight offset that caused by a force sensor (ZNLBS-VII-500, Ahznsensor, Ltd., Anhui, China) such that the lateral force can be measured as a compressive force. The force sensor has a measurement range of ± 5 N along its sensing axis with 0.001-N resolution. Fig. 9 indicates that the manipulator could generate a force laterally without changing its configuration, but under extra amount of tendon actuation. The result indicates a linear relationship between tendon actuation and measured force.

The stiffening mechanism is established on the assumption that the extra tendon actuation—compared to the inversely computed actuation according to the task space—would cause a minor axial compression that is imperceptible.

Besides, we examined how different initial configuration and axial payload can affect the end-effector positioning in response of the extra actuation for stiffening (see the result in Fig. 10). In the experiment, the soft robot was posed in different initial

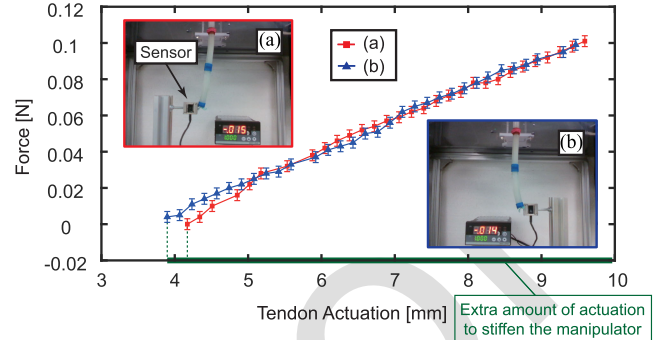


Fig. 9. Lateral pushing force measurement when the robot tendons were overactuated. The error-bar represents the measurement error of force sensor, which is 0.3%.

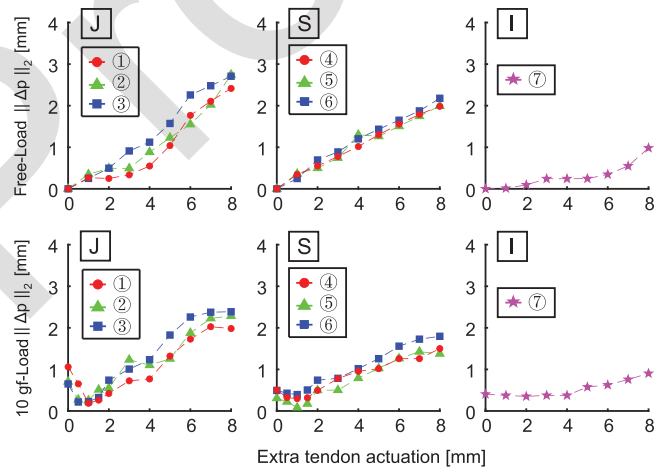


Fig. 10. Deviation of tip position affected by the proposed tendon tensioning method w.r.t. the desired position. The first row is in free load, and the second row is loaded with a 10-g axial force at the tip. Different initial configurations are considered, including the J-shape, S-shape, and I-shape (i.e., straight). Initial tip position is p_t^{RCM} : ① $\approx [-11.7, -2144.9]^T$, ② $\approx [-16.8, -6143.4]^T$, ③ $\approx [-13.6, -3143.9]^T$, ④ $\approx [-11.5, 7144.3]^T$, ⑤ $\approx [13.2, 7143.8]^T$, ⑥ $\approx [3.5, 5145.3]^T$, and ⑦ $\approx [-1.628, 1145.8]^T$ (unit: mm).

shapes, including J-, S-, and I-configuration. Extra tendon actuation (from 1–8 mm) was applied to the tendons to stiffen the robot. An RGB-D camera was used to measure the deviation of tip position from its desired one under both free load and 10-g load. All cases show a slight tip positioning error within 3 mm in Euclidean distance. The S-pose performs less error than that of the J-shape, and the straight pose demonstrates the least change. The loaded cases depict smaller errors than the free-loaded cases under the same configuration since the axial load (that axially scratching the robot) can partially cancel out the tendon actuation that axially compressing the manipulator. The results show that the optimal extra tendon actuation that can lower the tip positioning error falls in the range of [0,2] mm. Within a reasonable limit, the proposed stiffening method would not generate a major tip positioning error of our soft-bodied robot prototype. The minor error can be even smaller in the S-pose and I-pose.

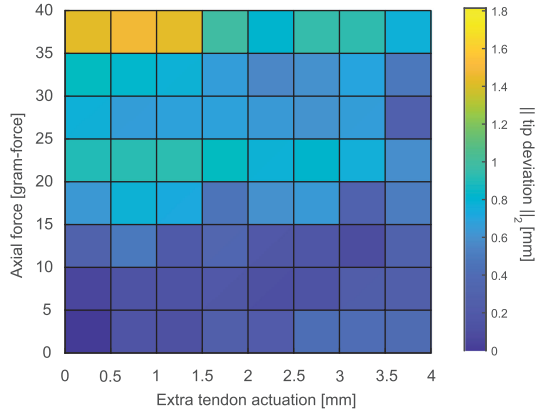


Fig. 11. Deviation map of the end-effector under different payload with extra tendon actuation. Upper left corner: without the tendon-tensioning stiffness adjustment, the axial force would generate large error of the tip. Upper right: with the tendon-tensioning stiffness adjustment, the error would be reduced. Lower right: the method will not generate major error.

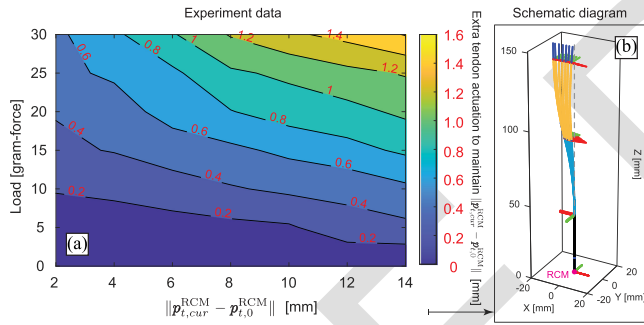


Fig. 12. (a) Mapping between the distance of the end-effector to the center and the corresponding minimum extra tendon actuation for stiffening the robot to maintain the desired tip position in different payload conditions. (b) Schematic diagram of the experiment.

In particular, we further examined the spatial deviation of end-effector subjected to different axial payload when it is at the initial configuration of “S.-.” As depicted in Fig. 11, we gradually added the axial load at the robot tip in different amount of extra tendon actuation with its initial tip position at $\mathbf{p}_t^{\text{RCM}} = [11.05, 1144.57]^T$. A higher level of tensioning, i.e., a stiffer soft robot body, demonstrates a better performance to resist the external force.

Based on the prototype experiment, Fig. 12(a) investigates the relationship between the distance of the end-effector to the working surface center (perpendicular to the Z-axis of RCM) and the needed minimum extra tendon actuation to maintain such distant position in different payload conditions. For the ease of understanding, a schematic diagram is given in Fig. 12(b) by simulation. The result indicates a nonlinear correlation among these three variants. When the desired position is farther away from the center (larger path), the soft manipulator is more sensitive to the disturbance, so that larger compensation would be required to maintain the position. In a trajectory tracking task, when the desired path is not a circle (i.e., not every point shares the same distance to the center), the minimum tendon compensation shall be iteratively updated. An example of tip path tracking is given in Fig. 13, where the desired path is a square isometrically divided

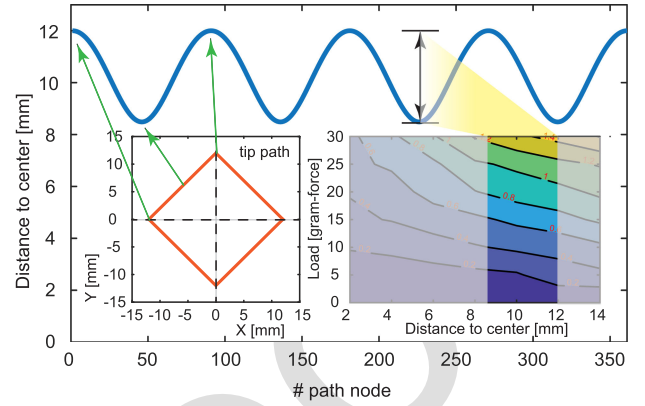


Fig. 13. Example of path distance to the working plane center. It necessitates different stiffness to maintain the tip position along the tracking in different payload condition.

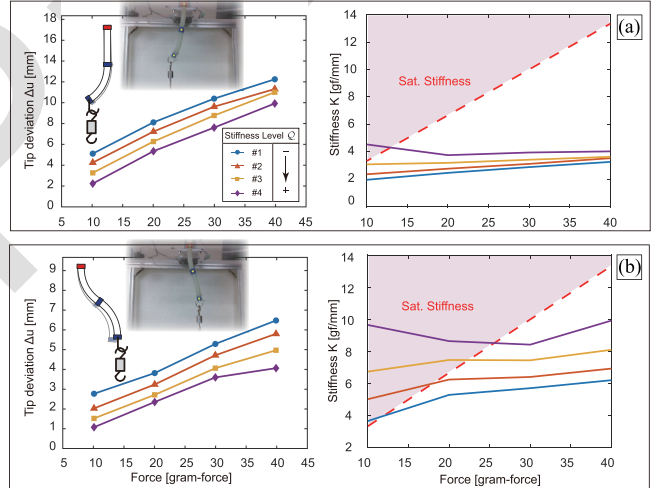


Fig. 14. Initial positions of the tip are: (a) $\mathbf{p}_t^{\text{RCM}} = [-19.284, 0145.097]^T$ and (b) $\mathbf{p}_t^{\text{RCM}} = [13.725, 0148.014]^T$ (unit: mm). The right column figures plot the correlation between manipulator stiffnesses and static forces, where the reddish regions represent the “satisfactory” stiffnesses that allow a tip perturbation within 3 mm.

by 360 nodes. Without prior knowledge of the load, the required actuation for optimal stiffness is changing along with the change of the tip position. Therefore, it necessitates the closed-loop control for the tendon compensation for variable stiffness.

To show the axial stiffening by tendon tensioning in different configurations, metal weights were hooked at the robot tip to deviate the tip positioning under different stiffness levels. As shown in Fig. 14, we measured the tip perturbation under four stiffness levels using four loads. Hooke’s law implies that the perturbation can be infinitesimal when the stiffness is infinite, i.e., completely rigid. Therefore, we set a satisfactory tip deviation of 3 mm based on the sensitivity of the depth vision and correlated a satisfactory stiffness that can correct the robot tip to its original position. The results show the following.

- 1) The robot stiffness can be enhanced by synergistically tensioning the tendons.
- 2) A stiffer rigidity mode shares a larger overlapped range with the satisfactory stiffness.

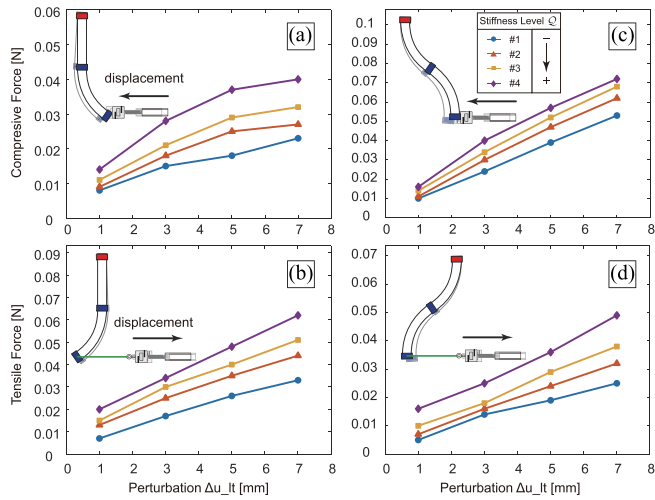


Fig. 15. Probe was mounted on a motor-driven linear slide. The lateral force was generally increased when the manipulator was stiffened, implying that the soft robot can be hardened in the lateral direction.

514 3) The S-configurations exhibit higher stiffness than that of
515 the J-configuration in the presence of axial load.

516 The results also indicate that the proposed method can stand
517 alone from the robot task space to control the robot stiffness.

518 To demonstrate that the lateral stiffness can be tuned by
519 tendon tensioning, we mounted a force sensor at the tip of a
520 home-made probe, which was secured on a motor-driven linear
521 slide to perturb the configured manipulator (i.e., in different
522 configurations, such as J- or S-shape) by a known displacement
523 with different tensioning mode and collected the compressive
524 force data. Likewise, another demonstration of tuning lateral
525 stiffness was conducted by reading tensile force, where the robot
526 tip and the sensor were connected by a fishing line, and a known
527 displacement, opposing to the direction of the previous test, was
528 given to the slide such that the probe could measure the tensile
529 force. The forces were recorded for every 2-mm perturbation
530 from 1 to 7 mm. The main idea was to stiffen the manipulator
531 so that it would show more resistance against the perturbation.
532 The results are plotted in Fig. 15, where different stiffening
533 levels were applied to enhance the lateral stiffness with the
534 initial configuration unchanged. The results confirm that the
535 lateral stiffness can be enhanced from the initial actuation by
536 our presented tensioning method, and also justify the compliance
537 nature of our variable-stiffness soft robot—it can be stiffened to
538 a competent level for the manipulation purpose without losing
539 the high compliance to ensure the safety to the possible collision.
540 This feature would be appreciated in the scene of human–robot
541 interaction, such as R-MIS.

542 To this extent, the effectiveness of the proposed stiffening
543 approach for the tendon-driven soft robot is validated. From
544 Figs. 8 and 9, it can be seen that the measured force and tip
545 deviation were not perfectly equally distributed even the robot
546 was in a symmetrical motion, inferring that the stiffness of
547 the soft body is subjected to various unquantifiable factors. It
548 motivates the adoption of the closed-loop method to fine-tune
549 the manipulator stiffness, as described in Section II-D.

B. Tip Trajectory Tracking With Loading

550 With continuously defined waypoints for tip path and on
551 the basis of Section II-D, the soft manipulator can perform tip
552 trajectory tracking with a vision-based stiffness tuning when it
553 is subjected to external loads.

554 Several experiments were conducted with an empirically set
555 trigger threshold of $\varepsilon = 3$ mm and buffer of $\lambda = 0.2$. The com-
556 parison of the performances of tracking different trajectories in
557 different conditions is given in Fig. 16. It can be seen that when a
558 payload was added to the manipulator, the operational trajectory
559 would be deviated from its desired trajectory, and such devia-
560 tion would be enlarged with increasing payload (see Fig. 17).
561 However, when utilizing the proposed stiffness compensation
562 scheme, the tip could provide the tracking performances, which
563 were as good as that of the open-loop mode without payload. As
564 shown in Fig. 17, the tracking performances were significantly
565 improved especially with larger payloads. The method allows
566 the robot to adjust its tendon actuation along the trajectory
567 without knowing how much payload it was holding. The cor-
568 recting processes could be done within one trajectory loop. In
569 the experiment, we conducted three trials for each trajectory in
570 different payload condition (10, 20, and 30 gf), and collected the
571 root-mean-square error (RMSE) of tip positioning and angular
572 deviation from the desired path (see Table II). Supported by
573 the experiment results, the average stiffness of the robot along
574 the trajectory can be approximated using the force and position
575 information ($\frac{K^* - K}{K}$), and this method can enhance the stiffness
576 by 132% for a square trajectory under an axial force of 30 gf. In
577 addition, as shown in Fig. 18, experiment results indicate that
578 the proposed method can be employed in tracking trajectory in
579 different sizes accurately in loaded cases.

IV. DISCUSSION

581 This article innovates the soft-bodied robot with an addi-
582 tional DOF by safely controlling its stiffness during the oper-
583 ational process. The proposed stiffening method demonstrates
584 several advantages over the other manipulator stiffening meth-
585 ods/mechanisms, which are listed in Table I, including the
586 following.

A. Applicability

588 Without complicated design and implementation of onboard
589 sensors or specially designed stiffening mechanism (e.g., stuff-
590 ing granular, jamming, etc.), which makes our method rapidly
591 applicable to many other existing tendon-driven soft robot sys-
592 tems with just an additional depth camera. The method provides
593 an inexpensive solution to upgrade many existing soft robots to
594 variable-stiffness versions.

B. Continuity

596 The method is applicable in some common scenarios where
597 the closed-loop feedback is not necessarily continuous. For
598 instance, in R-MIS, the sensory feedback is not always avail-
599 able throughout the course of the closed-loop manipulation.
600 In conventional visual servoing methods [34], [35], the system

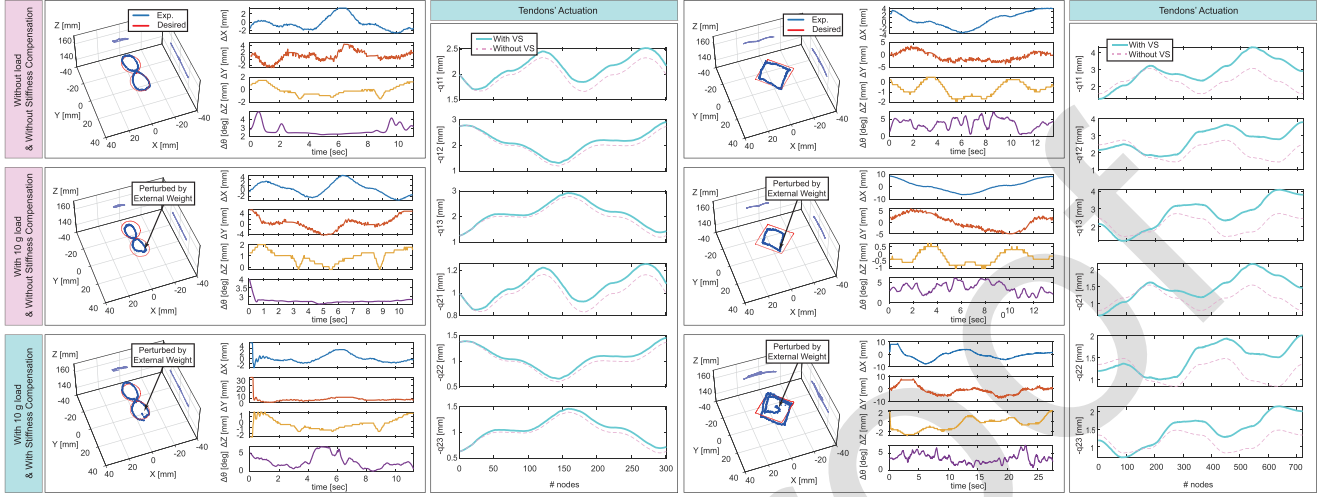


Fig. 16. Trajectory tracking performances of the open-loop control in free load (first row) and in 10-g load (second row), and with variable-stiffness control in 10-g load (third row).

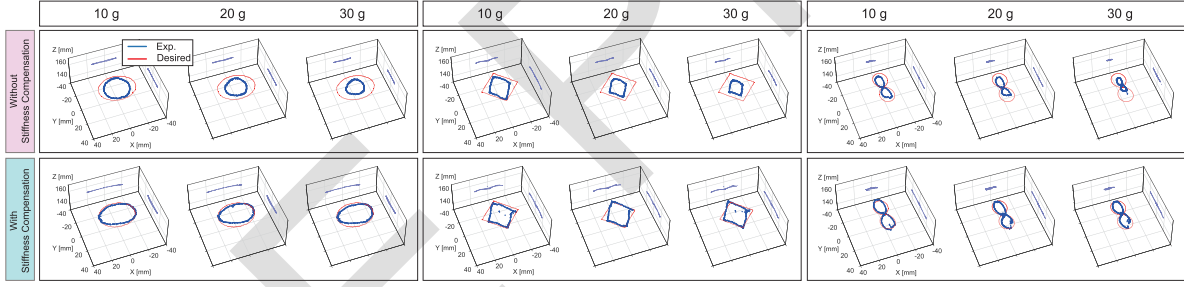


Fig. 17. Trajectory tracking performances of open-loop control (pink row) and with variable-stiffness control (green row) under different payload conditions.

TABLE II
RMSES OF TRACKING DIFFERENT TRAJECTORIES (SEE FIG. 17) IN THREE TRIALS

Tip Trajectory	\circ			\square			∞		
	10	20	30	10	20	30	10	20	30
Axial Load (gram-force)	10	20	30	10	20	30	10	20	30
RMSE of x_{RCM}^R (mm)	3.058 (4.964)	3.330 (6.305)	3.325 (7.389)	2.799 (4.831)	2.833 (6.234)	3.144 (7.201)	1.593 (2.313)	2.409 (2.633)	2.468 (3.331)
RMSE of y_{RCM}^R (mm)	3.170 (3.121)	2.890 (4.153)	2.870 (5.071)	2.740 (3.109)	2.361 (4.703)	2.245 (5.715)	2.689 (3.037)	2.510 (3.613)	3.220 (6.055)
RMSE of z_{RCM}^R (mm)	0.885 (0.969)	0.778 (1.369)	0.836 (1.656)	0.905 (0.614)	0.909 (0.829)	0.962 (1.011)	0.882 (0.579)	0.704 (0.726)	0.763 (1.391)
RMSE of Θ (°)	5.539 (3.148)	4.528 (2.688)	3.347 (2.579)	3.031 (3.970)	3.320 (3.589)	3.399 (3.489)	1.277 (3.393)	3.401 (2.345)	2.824 (1.814)
Stiffness Enhanced Avg. (%)	32.29	71.38	103.89	43.73	106.73	132.32	18.89	27.61	70.76

⁰Note: The values in bracket denote the reference values without stiffness compensation. The above trajectory shapes are in a size of 20 mm in either x - or y -axis.

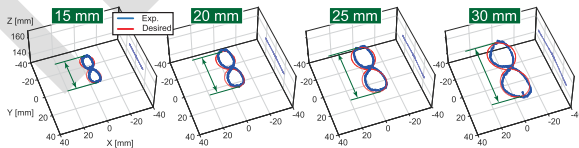


Fig. 18. Under the same axial force (10 gf), the stiffness-adaptiveness scheme fits well in different sizes of trajectory from 15 to 30 mm.

shall compute the visually available error in each loop to ensure the closed-loop control. However, the Jacobian update could be disturbed in some critical cases where the vision is lacking continuity. Thus, it ought to be switched to the open-loop mode. When it switches to the open-loop control, it can eventually

result in a large error in terms of tip positioning, and it can be even worse when the disturbances are introduced. In our method, the trajectory tracking task is based on an open-loop control, whereas the robot stiffness is secured by the closed-loop visual feedback. The experiments in Section III-B illustrate that the stiffness was iteratively accumulated. Even though the vision was blocked, the manipulator can still work as it was on the correct track based on the latest-optimized actuation without large error.

C. Adaptivity

The stiffening method is result-based, which does not require prior knowledge of the external payload. Within the payload

607
608
609
610
611
612
613
614
615

616
617
618

capacity, the robot could fine-tune its stiffness to adapt to the external force without excessive deflections. As depicted from the experimental results, the method would not result in an infiniteness of the stiffness. A balance of stiff and soft can be reached.

However, since the method requires the robot to be quasi-static, the momentum caused by introducing a weight to the manipulator when it was in motion would reduce the tip positioning accuracy. Therefore, a slower motion would be preferred. Besides, the method limits the stiffness variability to either the proximal segment or to the whole manipulator. Moreover, the tendon-driven mechanism without tendon pushing does not allow the stiffness compensation for the external force that axially compresses the manipulator.

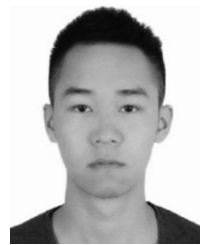
V. CONCLUSION

In this work, we propose a tendon-tensioning scheme to upgrade a normal dual-segment soft robot to a variable-stiffness version. It is experimentally confirmed that the proposed scheme can variate the stiffness of a soft robot, i.e., providing an additional controllable DOF to the robot, without apparent change in configuration. In the application of trajectory tracking, depth vision was employed to acquire the spatial deviation of the end-effector caused by an axial payload. The visual perception of the tip was treated as the closed-loop feedback for stiffness compensation. Utilizing our method, the manipulator can stabilize its instantaneous configuration by adaptively controlling its stiffness without losing its compliance. Extensive experiments were conducted to verify the principle of the tendon-tensioning method, and the antisturbance performance was also evaluated through the real-time trajectory tracking tests by adhering different payloads to the robot tip. The results indicate a significant improvement in terms of load-bearing trajectory tracking compared to the pure open-loop version, with a stiffness controllability up to 132%. The positioning error can be reduced up to 50% when with an external payload of 30 gf. And it can be inferred that the reduction would be more notable with heavier loads. This work shows that soft-bodied robots are having a great potential for the application in the future R-MIS manipulation for safer human–robot interaction.

REFERENCES

- [1] D. Rus and M. T. Tolley, "Design, fabrication and control of soft robots," *Nature*, vol. 521, no. 7553, pp. 467–475, 2015.
- [2] J. Burgner-Kahrs, D. C. Rucker, and H. Choset, "Continuum robots for medical applications: A survey," *IEEE Trans. Robot.*, vol. 31, no. 6, pp. 1261–1280, Dec. 2015.
- [3] R. J. Webster III and B. A. Jones, "Design and kinematic modeling of constant curvature continuum robots: A review," *Int. J. Robot. Res.*, vol. 29, no. 13, pp. 1661–1683, 2010.
- [4] M. Mahvash and P. E. Dupont, "Stiffness control of surgical continuum manipulators," *IEEE Trans. Robot.*, vol. 27, no. 2, pp. 334–345, Apr. 2011.
- [5] C. Li, X. Gu, X. Xiao, C. M. Lim, and H. Ren, "Flexible robot with variable stiffness in transoral surgery," *IEEE/ASME Trans. Mechatronics*, vol. 25, no. 1, pp. 1–10, Feb. 2019.
- [6] B. Ouyang, H. Mo, H. Chen, Y. Liu, and D. Sun, "Robust model-predictive deformation control of a soft object by using a flexible continuum robot," in *Proc. IEEE/RSJ Int. Conf. Intell. Robot. Syst.*, 2018, pp. 613–618.
- [7] L. Blanc, A. Delchambre, and P. Lambert, "Flexible medical devices: Review of controllable stiffness solutions," *Actuators*, vol. 6, no. 3, 2017, Art. no. 23.
- [8] S. P. Timoshenko and J. M. Gere, *Theory of Elastic Stability*. Chelmsford, MA, USA: Courier Corporation, 2009.
- [9] J. Shintake, B. Schubert, S. Rosset, H. Shea, and D. Floreano, "Variable stiffness actuator for soft robotics using dielectric elastomer and low-melting-point alloy," in *Proc. IEEE/RSJ Int. Conf. Intell. Robot. Syst.*, 2015, pp. 1097–1102.
- [10] A. Lendlein and R. Langer, "Biodegradable, elastic shape-memory polymers for potential biomedical applications," *Science*, vol. 296, no. 5573, pp. 1673–1676, 2002.
- [11] J. Peters *et al.*, "Actuation and stiffening in fluid-driven soft robots using low-melting-point material," in *Proc. IEEE/RSJ Int. Conf. Intell. Robot. Syst.*, 2019, pp. 4692–4698.
- [12] A. Jiang *et al.*, "Robotic granular jamming: Does the membrane matter?," *Soft Robot.*, vol. 1, no. 3, pp. 192–201, 2014.
- [13] M. Brancadoro, M. Manti, S. Tognarelli, and M. Cianchetti, "Fiber jamming transition as a stiffening mechanism for soft robotics," *Soft Robot.*, vol. 7, no. 6, pp. 663–674, 2020.
- [14] T. Ranzani, M. Cianchetti, G. Gerboni, I. De Falco, and A. Menciassi, "A soft modular manipulator for minimally invasive surgery: Design and characterization of a single module," *IEEE Trans. Robot.*, vol. 32, no. 1, pp. 187–200, Feb. 2016.
- [15] Y.-J. Kim, S. Cheng, S. Kim, and K. Iagnemma, "A novel layer jamming mechanism with tunable stiffness capability for minimally invasive surgery," *IEEE Trans. Robot.*, vol. 29, no. 4, pp. 1031–1042, Aug. 2013.
- [16] T. Wang, J. Zhang, Y. Li, J. Hong, and M. Y. Wang, "Electrostatic layer jamming variable stiffness for soft robotics," *IEEE/ASME Trans. Mechatronics*, vol. 24, no. 2, pp. 424–433, Apr. 2019.
- [17] A. Stilli, H. A. Wurdemann, and K. Althoefer, "A novel concept for safe, stiffness-controllable robot links," *Soft Robot.*, vol. 4, no. 1, pp. 16–22, 2017.
- [18] A. J. Loeve, D. H. Plettenburg, P. Breedveld, and J. Dankelman, "Endoscope shaft-rigidity control mechanism: 'Forguide,'" *IEEE Trans. Biomed. Eng.*, vol. 59, no. 2, pp. 542–551, Feb. 2012.
- [19] Y. Zhong, R. Du, P. Guo, and H. Yu, "Investigation on a new approach for designing articulated soft robots with discrete variable stiffness," *IEEE/ASME Trans. Mechatronics*, early access, Jan. 06, 2021, doi: 10.1109/TMECH.2021.3049592.
- [20] I. Tamadon, Y. Huan, A. G. de Groot, A. Menciassi, and E. Sinibaldi, "Positioning and stiffening of an articulated/continuum manipulator for implant delivery in minimally invasive surgery," *Int. J. Med. Robot. Comput. Assisted Surgery*, vol. 16, no. 2, 2020, Art. no. e2072.
- [21] A. Degani, H. Choset, A. Wolf, and M. A. Zenati, "Highly articulated robotic probe for minimally invasive surgery," in *Proc. IEEE Int. Conf. Robot. Autom.*, 2006, pp. 4167–4172.
- [22] Y.-J. Kim, S. Cheng, S. Kim, and K. Iagnemma, "A stiffness-adjustable hyperredundant manipulator using a variable neutral-line mechanism for minimally invasive surgery," *IEEE Trans. Robot.*, vol. 30, no. 2, pp. 382–395, Apr. 2014.
- [23] A. Shiva *et al.*, "Tendon-based stiffening for a pneumatically actuated soft manipulator," *IEEE Robot. Autom. Lett.*, vol. 1, no. 2, pp. 632–637, Jul. 2016.
- [24] M. Cianchetti *et al.*, "Soft robotics technologies to address shortcomings in today's minimally invasive surgery: The stiff-flop approach," *Soft Robot.*, vol. 1, no. 2, pp. 122–131, 2014.
- [25] J. Lai, K. Huang, B. Lu, and H. K. Chu, "Toward vision-based adaptive configuring of a bidirectional two-segment soft continuum manipulator," in *Proc. IEEE/ASME Int. Conf. Adv. Intell. Mechatronics*, 2020, pp. 934–939.
- [26] T. Kato, I. Okumura, S.-E. Song, A. J. Golby, and N. Hata, "Tendon-driven continuum robot for endoscopic surgery: Preclinical development and validation of a tension propagation model," *IEEE/ASME Trans. Mechatronics*, vol. 20, no. 5, pp. 2252–2263, Oct. 2015.
- [27] J. Ding, R. E. Goldman, K. Xu, P. K. Allen, D. L. Fowler, and N. Simaan, "Design and coordination kinematics of an insertable robotic effectors platform for single-port access surgery," *IEEE/ASME Trans. Mechatronics*, vol. 18, no. 5, pp. 1612–1624, Oct. 2013.
- [28] J. Lai, K. Huang, B. Lu, Q. Zhao, and H. K. Chu, "Verticalized-tip trajectory tracking of a 3D-printable soft continuum soft robot: Enabling surgical blood suction automation," under review, 2020.
- [29] K. Xu and N. Simaan, "An investigation of the intrinsic force sensing capabilities of continuum robots," *IEEE Trans. Robot.*, vol. 24, no. 3, pp. 576–587, Jun. 2008.

- 750 [30] D. Zhalmuratova and H.-J. Chung, "Reinforced gels and elastomers for
751 biomedical and soft robotics applications," *ACS Appl. Polym. Mater.*, vol. 2,
752 no. 3, pp. 1073–1091, 2020.
753 [31] F. F. Abayazid and M. Ghajari, "Material characterisation of additively
754 manufactured elastomers at different strain rates and build orientations,"
755 *Additive Manuf.*, vol. 33, 2020, Art. no. 101160.
756 [32] M. C. Yip and D. B. Camarillo, "Model-less feedback control of continuum
757 manipulators in constrained environments," *IEEE Trans. Robot.*, vol. 30,
758 no. 4, pp. 880–889, Aug. 2014.
759 [33] H. Wang, M. Totaro, and L. Beccai, "Toward perceptive soft robots:
760 Progress and challenges," *Adv. Sci.*, vol. 5, no. 9, 2018, Art. no. 1800541.
761 [34] H. Wang, B. Yang, Y. Liu, W. Chen, X. Liang, and R. Pfeifer, "Visual
762 servoing of soft robot manipulator in constrained environments with an
763 adaptive controller," *IEEE/ASME Trans. Mechatronics*, vol. 22, no. 1,
764 pp. 41–50, Feb. 2017.
765 [35] F. Xu, H. Wang, J. Wang, K. W. S. Au, and W. Chen, "Underwater dynamic
766 visual servoing for a soft robot arm with online distortion correction,"
767 *IEEE/ASME Trans. Mechatronics*, vol. 24, no. 3, pp. 979–989, Jun. 2019.



768 **Jiewen Lai** (Student Member, IEEE) received the B.Eng. degree in metallurgical engineering
769 from the Wuhan University of Science and Technology, Wuhan, China, in 2016, and the M.Sc.
770 degree in mechanical and automation engineering from The Chinese University of Hong Kong,
771 Hong Kong, in 2017. He is currently working toward the Ph.D. degree in mechanical engineering
772 with The Hong Kong Polytechnic University, Hong Kong.
773 His research interests include soft/continuum
774 robot and surgical robot system.
775
776
777
778
779
780



781 **Bo Lu** received the B.Eng. degree in ship and
782 offshore engineering from the Dalian University
783 of Technology, Dalian, China, in 2013, and the
784 M.S. and Ph.D. degrees from The Hong Kong
785 Polytechnic University, Hong Kong, in 2015 and
786 2019, respectively, both in mechanical engineering.
787

788 He is currently a Postdoctoral Research Fellow
789 with the T Stone Robotics Institute, The
790 Chinese University of Hong Kong, Hong Kong.
791 His current research interests include medical
792 robotics, computer vision, and surgical automation technique.
793



794 **Henry K. Chu** (Member, IEEE) received the
795 B.S. degree in mechanical engineering from the
796 University of Waterloo, Waterloo, ON, Canada,
797 and the M.S. and Ph.D. degrees from the University
798 of Toronto, Toronto, ON, Canada, both in
799 mechanical and industrial engineering.
800

801 He was a Postdoctoral Fellow with the University
802 of Toronto and the City University of Hong
803 Kong, Hong Kong. He is currently an Assistant
804 Professor with The Hong Kong Polytechnic
805 University, Hong Kong. His research interests
806 include robotic manipulation, vision-based control and automation,
807 microsystem design, and tissue engineering.
808